

RESEARCH ARTICLE | APRIL 07 2025

A compact multi-degree-of-freedom piezoelectric motor with large travel capability

Syed Asad Maqbool  ; Muhammad Touqeer  ; Behnam Esmaeilzadeh  ; Shiwei Yang; Wenjie Meng  ; Jihao Wang  ; Qiyuan Feng; Yubin Hou  ; Qingyou Lu  



Rev. Sci. Instrum. 96, 043702 (2025)

<https://doi.org/10.1063/5.0240886>



Articles You May Be Interested In

A multi-degree-of-freedom model-based method for Young's modulus determination of soft tissue by resonance spectroscopy

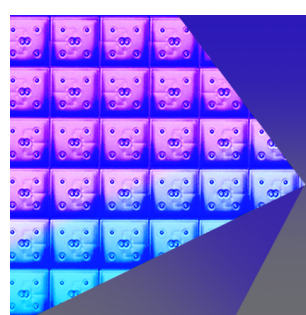
Appl. Phys. Lett. (February 2025)

Magnetic field analysis of a hybrid excitation multi-degree-of-freedom spherical motor

Rev. Sci. Instrum. (November 2022)

Dynamic characteristics and response of low frequency cantilever beam-based FBG accelerometer under base excitation

AIP Conf. Proc. (January 2019)



**Review of
Scientific Instruments**
Special Topics Now Online

[Learn More](#)

 AIP
Publishing

A compact multi-degree-of-freedom piezoelectric motor with large travel capability

Cite as: Rev. Sci. Instrum. 96, 043702 (2025); doi: 10.1063/5.0240886

Submitted: 27 September 2024 • Accepted: 27 February 2025 •

Published Online: 7 April 2025



View Online



Export Citation



CrossMark

Syed Asad Maqbool,^{1,2} Muhammad Touqeer,^{1,2} Behnam Esmaeilzadeh,^{1,2} Shiwei Yang,^{1,2}
Wenjie Meng,^{2,3} Jihao Wang,^{2,3} Qiyuan Feng,^{2,3} Yubin Hou,^{2,3} and Qingyou Lu^{1,2,3,4,a)}

AFFILIATIONS

¹ Hefei National Laboratory for Physical Sciences at the Microscale, University of Science and Technology of China, Hefei 230026, People's Republic of China

² High Magnetic Field Laboratory, Hefei Institutes of Physical Science, Chinese Academy of Sciences, Hefei, Anhui 230031, China

³ Anhui Key Laboratory of Low-Energy Quantum Materials and Devices, High Magnetic Field Laboratory, Hefei Institutes of Physical Science, Chinese Academy of Sciences, Hefei, Anhui 230031, China

⁴ Anhui Laboratory of Advanced Photon Science and Technology, University of Science and Technology of China, Hefei, Anhui 230026, China

^{a)}Author to whom correspondence should be addressed: qxl@ustc.edu.cn

ABSTRACT

This study introduces a novel multi-degree-of-freedom (MDOF) piezoelectric motor (PEM) for high precision and a $10 \times 10 \text{ mm}^2$ large travel range within a rigid and compact structure ($33 \times 33 \times 30 \text{ mm}^3$). The motor consists of four piezoelectric tubes (PTs) arranged and mounted parallel to each other to enable controlled movement along both the X and Y axes by using a sawtooth waveform with a time-delay control strategy. The design features a moving plate clamped between two upper and two lower sapphire balls, with the balls supported by CuBe springs, ensuring symmetric and precise movement. Applying individual driving signals to each PT induces bending deformation sequentially in the same direction, followed by simultaneous recovery to the original position, thereby enabling the movement of the moving plate. Experimental results demonstrated that the motor operated effectively at a signal frequency of 150 Hz, with a minimum driving voltage of 18 V required for detectable motion. The motor exhibited the capability to produce step sizes from 0.53 to 6.23 μm with a linear relationship between driving voltage (± 30 to ± 180 V) and step size, ensuring consistent performance. The hysteresis analysis revealed minimal energy loss, with hysteresis ratios of 5.2% on the X axis and 4.16% on the Y axis, indicating the motor's high precision and efficiency. Additionally, the motor sustained a load of 120 g while traversing a $10 \times 10 \text{ mm}^2$ area, and continuous operation for 12 h revealed no significant performance degradation. The compact and reliable design of this novel MDOF PEM holds potential for applications in confined spaces, such as small-bore superconducting magnets, enabling precise large-area atomic resolution imaging and magnetic property measurements.

Published under an exclusive license by AIP Publishing. <https://doi.org/10.1063/5.0240886>

I. INTRODUCTION

Multi-degree-of-freedom (MDOF) piezoelectric motors (PEMs) are advanced devices that leverage the piezoelectric effect to produce precise and controlled movements in multiple directions. These motors are widely used in applications requiring high precision and fine control, such as in scanning probe microscopy, micro-robotics, precision engineering, and medical devices.^{1–6} The key advantages of MDOF PEMs include their ability to achieve high-resolution positioning, rapid response times, and the capability to operate in compact spaces without the need for complex

mechanical linkages.^{7–9} Additionally, they offer excellent repeatability and reliability, making them ideal for precision positioning systems in applications.^{10–12}

The increasing demand for precision positioning systems in applications has led to significant advancements in piezoelectric motors.¹³ These motors are favored for their high precision, compact size, and fast response time. However, conventional piezoelectric motors often face challenges related to hysteresis, energy loss, and durability under high-load and long-term operational conditions.¹⁴ Addressing these limitations is crucial to enhance their performance and extend their applicability.

To achieve high-precision results over a wide range of motion, several MDOF PEMs have been developed and utilized over the past several decades.^{15–17} However, the MDOF movement is typically generated by the superposition of several single-axis motions. These designs inherently limit the ability to maintain actuator consistency, as interactions between individual actuators can lead to disturbances, ultimately causing inefficiencies and reduced controllability of the motor. Although MDOF PEMs offer high precision, flexibility, and adaptability in various fields, particularly their ability to operate without electromagnetic interference and provide nanoscale resolution makes them ideal for cutting-edge technological applications. Therefore, some studies are focused on this field.

The resonance-free PEMs offer more flexible configurations and a broad frequency range of operation, as they function outside of resonant states.^{18,19} Stepping-type piezoelectric actuators are a key example of non-resonant piezoelectric actuators, such as inertial piezoelectric actuators, which achieve long strokes by sequentially accumulating micro-steps.^{20,21} However, the majority of current stepping piezoelectric actuators are limited to producing motion in only one dimension.^{14,22} There are few reports in the literature on MDOF piezoelectric motors, and most of them feature relatively complex designs. This complexity arises from the use of multiple single-DOF actuators arranged in different spatial directions. A two-DOF inertial rotary motor constructed by Zhang *et al.*²³ utilizes a stick-slip mechanism, resulting in limited load capacity (~ 0.53 mN m). Furthermore, slight discrepancies in displacement resolution along different axes are observed due to structural asymmetries. The platform developed by Liu *et al.*²⁴ uses longitudinal-bending hybrid actuators for two-dimensional motion. However, its complex structure, involving multiple PZT stacks and precise alignment requirements, increases the fabrication difficulty. Moreover, coupling effects during transitions can introduce undesired displacements, reducing positioning accuracy and high hysteresis. The motor proposed by Jin *et al.*²⁵ achieved MDOF motion using a fish-body-inspired structure. However, the structural asymmetry in the X and Y directions leads to differences in velocity between the two axes, which compromises uniform performance. Additionally, miniaturization of the motor reduces vibrational amplitude, limiting efficiency at smaller scales.

Nichols and Ng²⁶ introduced a two-DOF PEM, where the system's walker consists of six piezoelectric tubes (PTs), with one end of each tube fixed to a central macro-piece, while the opposite ends are connected to two sapphire disks. These disks press against both the top and bottom alumina plates. During operation, each PT deforms sequentially in the desired direction and then returns to its original state simultaneously. The motor achieved two-dimensional motion through the combined longitudinal and transverse deformations of the PTs. Although this design is compact and stable, it poses a challenge in ensuring that all six sapphire disk contact points lie on the same plane since only three points can definitively determine a plane. As a result, achieving uniform friction forces between the sapphire disks and alumina plates can be difficult, potentially rendering the device inoperable. In our group, Zheng *et al.*¹⁵ developed a two DOF PEM that utilizes a simple cross-shaped piezoelectric unit for effective operation. This novel design is characterized by its rigidity, compactness, and planar structure. However, the cross-shaped piezo-unit is situated between the top and bottom guiding plates, which should be equal pressing forces exerted on the four free ends

of the piezo-unit and the plates for uniform motion. Four sapphire clips are affixed to the edges, with two sapphire balls secured on the top and two on the bottom. The weight of the piezo-stacks on the bottom sapphire balls, however, disrupted the operation by generating unequal clamping forces compared to the top sapphire balls, resulting in non-uniform motion in X and Y planes. Additionally, the motor's overall diameter was not fit for confined spaces and the travel range was restricted along both the X and Y axes up to 8 mm, and it struggled to achieve consistent accuracy on both axes when under load due to the nonlinear behavior of the piezoelectric stacks, particularly due to high hysteresis and creep effect.^{27,28}

These MDOF PEMs face significant challenges in achieving large travel capability along the simple and compact design and achieving both high precision and durability, particularly under high-load or long-term operational conditions. Existing designs often suffer from high hysteresis ratios, leading to reduced accuracy, and excessive energy dissipation, limiting their efficiency. This study presents a novel MDOF PEM designed to overcome these challenges. To achieve high precision and a large travel range of up to 10×10 mm² along a symmetric and compact structure, we introduce a novel MDOF PEM design utilizing four PTs. The moving plate is clamped between two top and two bottom sapphire balls, which are indirectly connected to the PTs using copper beryllium springs, ensuring smooth and precise movement of the plate. The detailed configuration of the motor will be discussed in Sec. II. This motor combines high precision with a significant travel range of up to 1 cm on both X and Y axes while maintaining a compact size (33 × 33 × 30 mm³). This study demonstrates a significant advancement in the MDOF-PEM design and performance. The proposed motor achieves low hysteresis, high energy efficiency, and stable operation under high loads and prolonged use, addressing critical challenges in the field. These features make it ideal for precise positioning applications, especially in confined spaces, such as within small-bore superconducting magnets, enabling atomic resolution imaging or magnetic property measurements over precise large area.

II. STRUCTURE

The schematic design of our novel piezoelectric motor (PEM) is depicted in Fig. 1(a). The design features four piezoelectric tubes (PTs), each with a length of 28 mm, an external diameter of 8.27 mm, and a wall thickness of 1 mm. Each PT is equipped with four inner electrode segments and one outer electrode. The outer electrodes of all PTs are connected to a common ground signal by a micrometer-sized wire. The inner electrodes are glued with micrometer-sized wires using conductive silver epoxy (H20E, Epoxy Tech., USA). The PTs are affixed to a sapphire circular base (diameter of 25.25 mm) using insulated epoxy (H74E). The PTs are arranged in a parallel configuration and are inserted into four precisely machined holes with a diameter of 8.32 mm that are located on the sapphire base. Furthermore, the base contains a few smaller holes with a diameter of 2 mm to enable the passage of electrical wires, as shown in Fig. 1(a). Each PT contained four inner electrodes, which are aligned along specific directions. The arrangement of these tubes is designed to ensure that all electrodes are oriented symmetrically relative to a common coordinate system. The electrodes of each tube are aligned in a symmetrical pattern such that

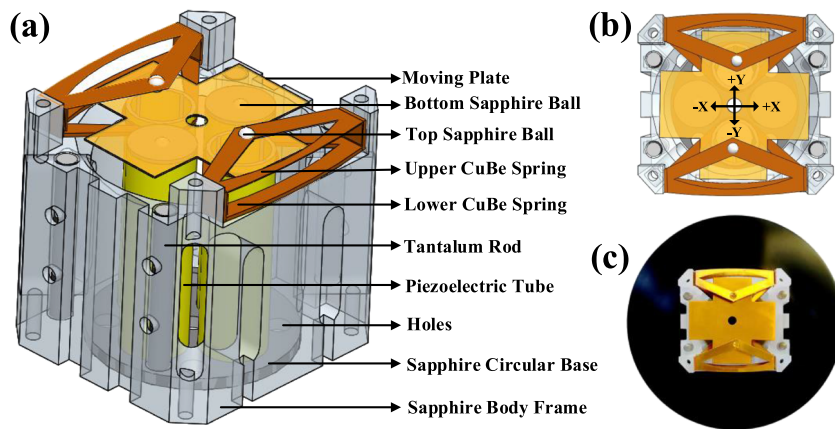


FIG. 1. (a) Schematic illustration of PEM. (b) Top view of PEM along XY axes selected during the experiment. (c) Top view of a prototype of PEM.

- One electrode is aligned in the +X direction.
- One electrode is aligned in the -X direction.
- One electrode is aligned in the +Y direction.
- One electrode is aligned in the -Y direction.

This configuration ensures that when driving signals are applied to the electrodes, the resulting forces on the moving plate will be symmetrical and controlled. To ensure a strong connection between the PTs and the sapphire base, the assembly is heated in a microwave at 85 °C for 150 min, and the resulting is called the PT unit. Next, the PT assembly is attached to a sapphire body frame ($33 \times 33 \times 30 \text{ mm}^3$) using washable glue, which allows for easy disassembly if needed. Four tantalum rods (2.50 mm in diameter and 20 mm in length) are inserted into specific holes in the sapphire frame and tightly screwed in place. These rods added weight to the motor, which is essential for enhancing stability and reducing vibrations during operation. Small sapphire disks (8.27 mm in diameter and 1 mm thick) with a central hole (1.9 mm in diameter) are used to secure sapphire balls (2 mm in diameter), which are then mounted on top of two of the PTs. Springs made of copper beryllium (CuBe) with a thickness of 0.5 mm are attached to the other two PTs so that when PT deforms, CuBe springs ensures uniform clamping force across the moving plate, effectively counterbalancing external forces and reducing nonlinear effects, such as creep, thereby enhancing stability and precision. The top of each PT is inserted into a spring hole (8.35 mm in diameter) and glued to create a strong connection between the PT and the spring. The plus-shaped moving plate, made of phosphor bronze (dimensions: $24 \times 24 \times 0.15 \text{ mm}^3$), is positioned on the PT unit, making contact only with the sapphire balls beneath it. Two additional CuBe springs (0.2 mm thick) having fixed sapphire balls are securely glued to the lower springs, effectively sandwiching the moving plate between the upper and lower springs. The upper springs, equipped with sapphire balls, apply downward force on the moving plate. This force is counterbalanced by the reaction forces from the lower sapphire balls, ensuring equilibrium. During this process, it was confirmed that the springs do not touch the sapphire body frame from any side.

Significantly, the motor's design includes only four contact points, each applying equal force, creating a stable equilibrium necessary for the motor's optimal operation. The 2-top-2-bottom

contacting structure ensures uniform clamping force on the moving plate. However, it is essential to control the blocking force generated by the upper springs to prevent any bending of the moving plate. Bending indicates that the blocking force exceeds the pushing force from the PTs, which would hinder the moving plate's mobility.

The moving plate must be frictionless and wear-resistant, which is why phosphor bronze, known for its excellent elasticity, wear resistance, and lightweight properties, was selected. Additionally, the surface of the moving plate is coated with a TiN film, providing sufficient static friction between the sapphire balls and the TiN-coated moving plate, ensuring smooth operation. This PEM also consists of four legs on top of the sapphire frame, which makes the specific travel area for the moving plate, and holes on the legs will be used for further study to construct STM or Magnetic Force Microscope (MFM) system. The overall dimensions of this PEM are $33 \times 33 \times 30 \text{ mm}^3$, and the overall diameter of motor is 41 mm. Figures 1(b) and 1(c) represent the top view of PEM along XY axes selected during the experiment and prototype of PEM, respectively.

III. WORKING PRINCIPLE

The working principle of the PEM relies on the precise control of frictional forces between the moving plate and sapphire balls. The motor is controlled using a sawtooth waveform with a time-delay-based control strategy as the driving signal. This driving signal has the amplitude ranges from ± 30 to $\pm 180 \text{ V}$ depending on the desired step size, and the frequency is fixed at 150 Hz, as determined from our experimental optimization to achieve efficient and precise operation. The steep rising edge of the sawtooth waveform induces rapid deformation of the PTs, while the gradual falling edge minimizes overshoot and ensures stability during retraction. To achieve multi-degree-of-freedom motion, a sequential activation strategy is applied to the four PTs. This strategy incorporates a precise time delay between the activation of each PT to create controlled bending and directional movement. The time delay between activations was optimized experimentally to ensure smooth, consistent motion and minimize interference between PTs. This delay allows the motor to maintain precise control of the moving plate's position while minimizing the impact of nonlinear effects such as hysteresis or creep.²⁹

Assume that by applying driving signals to electrodes positioned in the $-X$ direction of all PTs, controlled bending and frictional forces are exerted on the moving plate, enabling its mobility in the $+X$ direction. An example illustrating this simple working principle is shown in Fig. 2, with a detailed description provided below.

Step-1: In the initial step, a driving signal applied to the first PT induces bending in the $-X$ direction. This bending generates a frictional force between the moving plate and the sapphire ball in contact with the bent PT. However, if the other three PTs remain inactive, the static frictional forces ($FS_2 + FS_3 + FS_4$) between the moving plate and the three inactive sapphire balls are greater than the dynamic frictional force (FD_1) between the moving plate and the active sapphire ball due to the 1:3 ratio. Consequently, the moving plate remains stationary. The mathematical expression for this step is given as follows:

$$FD_1 < FS_2 + FS_3 + FS_4.$$

Step-2: In step 2, a driving signal applied to the second PT induces bending in the $-X$ direction after a specific time delay, while the first PT remains in a deformation state due to the imposed time delay in the first PT signal. However, as explained in step 1, the static frictional forces ($FS_1 + FS_3 + FS_4$) between the moving plate and the three inactive sapphire balls (i.e., those in contact with the non-activated PTs) still exceed the dynamic frictional force (FD_2) between the moving plate and the active sapphire ball (i.e., the one in contact with the activated PT). Therefore, despite the activation of the second PT, the moving plate remains immobile due to the dominant static frictional forces,

$$FD_2 < FS_1 + FS_3 + FS_4.$$

Step-3 and 4: In steps 3 and 4, driving signals are individually applied to the remaining PTs to induce bending in the

$-X$ direction. Similar to steps 1 and 2, the moving plate remains stationary in each step because the static frictional forces between the moving plate and the three inactive sapphire balls continue to be greater than the dynamic frictional force between the moving plate and the single active sapphire ball,

$$FD_3 < FS_1 + FS_2 + FS_4,$$

$$FD_4 < FS_1 + FS_2 + FS_3.$$

Step-5: In step 5, a retraction driving signal is simultaneously applied to all PTs, causing them to return to their original, unbent state. At this point, the dynamic frictional forces between the moving plate and all four sapphire balls become greater than the static frictional force. This is because the retraction signal reduces the normal force between the moving plate and the sapphire balls, thereby decreasing the static frictional force. As a result, the moving plate overcomes the static frictional resistance and moves one step in the $+X$ direction.

By precisely controlling the time delay and sequence of driving signals applied to the PTs, the PEM achieved precise and controlled movement of the moving plate in all directions. Due to the symmetrical structure of the PEM, the operating principle is consistent in all directions. This means that the same process of applying driving signals, generating frictional forces, and achieving movement steps applies regardless of the direction of motion, whether it is $+X$, $-X$, $+Y$, or $-Y$.

IV. EXPERIMENTAL RESULTS

To assess the characteristics and driving performance of this novel MDOF PEM, a series of experiments were conducted using the prototype within the setup depicted in Figs. 3(a) and 3(b). A custom-designed modular controller,³⁰ available commercially through CASMF Sci&Tech. Ltd., was employed to provide the precise control signals required by the motor. LabVIEW software was utilized to manage and optimize the PEM's performance, enabling

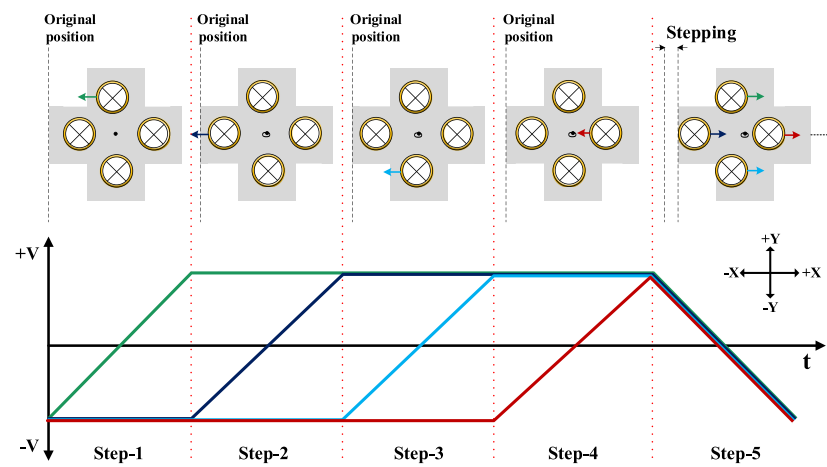


FIG. 2. Schematic diagram of the operating principle of PEM along sawtooth driving signals with a time-delay-based control strategy; small colored arrows show deforming directions of PTs, and the same colored lines show the driving signal of the related PTs.

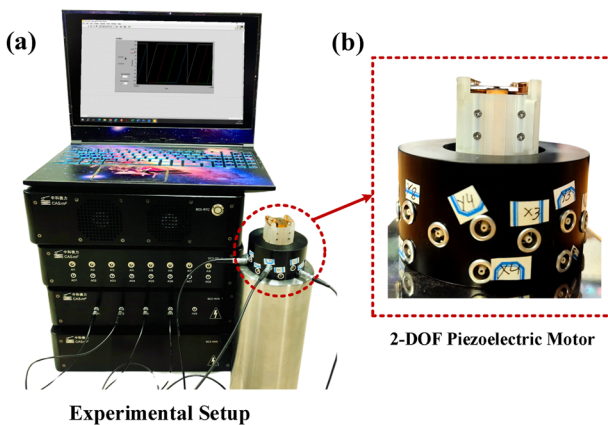


FIG. 3. (a) Experimental setup included a custom-designed modular controller, PC with LabVIEW software, and Piezoelectric Motor (PEM). (b) Photograph of PEM along a connector box.

the generation of arbitrary waveforms and controlled voltages up to 200 V. The displacement of the moving plate was continuously monitored using an optical microscope at 300 \times magnification (BYOM-018, Being Nano-Instruments, China).

To calculate the step size and velocity of the motor, a specific travel distance was defined for the moving plate, after which the number of steps was recorded and the average was computed in the +X, -X, +Y, and -Y directions. Once the motor's performance was optimized, the signal frequency was set at 150 Hz to determine the threshold voltage. It was observed that when the voltage reached 18 V, the movement of the plate became detectable in all directions, establishing 18 V as the minimum driving voltage (threshold voltage) for motion in the X and Y directions. Subsequently, the step size of the motor was measured in the +X, -X, +Y, and -Y directions by varying the voltage from 30 to 180 V while maintaining a constant signal frequency of 150 Hz. The results indicated [Fig. 4(a)] that the step size increased almost linearly from \sim 0.5 to 6 μ m as the voltage was varied from 30 to 180 V, confirming a linear correlation between driving voltage and step size across all directions.^{12,15} Notably, the step sizes remained consistent in all four directions, highlighting the symmetrical structure of the motor. Moreover, due to the non-inertial nature of the PEM,³¹ the linear trends in all directions were highly similar, ensuring high precision in stepping to cover a travel distance of 1 cm.

To ensure consistent performance and dynamic response of the PEM, step size and velocity were measured across varying frequencies while maintaining a constant driving voltage of 90 V, as depicted in Figs. 4(b) and 4(c). The results indicated that as the signal frequency increased, step sizes gradually decreased until reaching a threshold frequency of 150 Hz. Beyond this point, there were no significant variations in step size across all directions, likely due to the saturation of the PEM's mechanical response. At frequencies below 150 Hz, the PEM closely followed the input signal, but after surpassing this threshold frequency, the PTs could no longer respond quickly enough, leading to response saturation.^{12,32} Conversely, the velocity of the PEM increased linearly in all directions as the frequency increased. This behavior is attributed to the fact that

consistent displacement was achieved by the PEM during each input cycle, and increasing the frequency resulted in a higher number of these displacements per second, even at higher frequencies.

The positioning accuracy of smart PEMs is typically influenced by inherent nonlinearities, primarily due to hysteresis effects during dynamic operation.²³ In this study, the hysteresis behavior of this novel PEM was also evaluated. For this analysis, the operation time of the moving plate was fixed, and the displacements from the initial position were recorded as the cyclic driving voltage was varied between \pm 30 and \pm 180 V, while the frequency maintained at 150 Hz. This hysteresis loop represents the deviation between mean forward and mean reverse displacement paths and the relationship between cyclic driving voltage and output displacement along the X and Y plane, illustrated in Figs. 5(a) and 5(b), respectively. Hysteresis ratios can be calculated as follows:

$$\text{Hysteresis ratio} = \frac{\Delta d}{d_{\max}} \times 100,$$

where Δd is the maximum difference between the mean forward and mean reverse paths of the displacement–voltage curve and d_{\max} is the maximum output displacement at maximum voltage. This is found here that hysteresis ratios at the X and Y planes are 5.2% and 4.16%, respectively. Therefore, the hysteresis in the PEM is relatively small, which indicates a small amount of energy loss due to hysteresis, but the performance is relatively good.³³

Repeated uncertainty analysis was conducted to validate the reliability and consistency of the motor's performance. Herein, five sets of displacements are taken for both forward and reverse voltages and calculated mean value of displacement. These values are used in the following standard deviation relationship to calculate forward and reverse standard deviations at specific voltage:

$$\text{Std} = \sqrt{\frac{1}{n-1} \sum_{i=1}^n (d_i - \bar{d})^2},$$

where n is the number of sets, d_i is the represented displacement, Std is the standard deviation, and \bar{d} is the mean displacement at specific voltage. Hysteresis uncertainty at specific voltage can be calculated as follows:

$$\text{Hysteresis uncertainty } (\sigma) = \sqrt{(\text{Forward Std})^2 + (\text{Reverse Std})^2}.$$

From this relationship, we got uncertainty at specific voltage. The overall uncertainty in hysteresis performance was calculated using the Root Mean Square (rms) method,

$$\text{Overall Uncertainty } (\sigma_{\text{RMS}}) = \sqrt{\frac{1}{n} \sum_{i=1}^n \sigma_i^2},$$

where n is the total number of hysteresis uncertainty and σ_i is the individual hysteresis uncertainty value at specific voltage. The overall uncertainty in percentage at X and Y planes can be obtained as follows:

$$\text{Uncertainty } (\%) = \frac{\sigma_{\text{RMS}}}{d_{\max}} \times 100,$$

where d_{\max} is the maximum displacement in one complete cycle. Hence, the uncertainty in hysteresis ratios was calculated as 0.62%

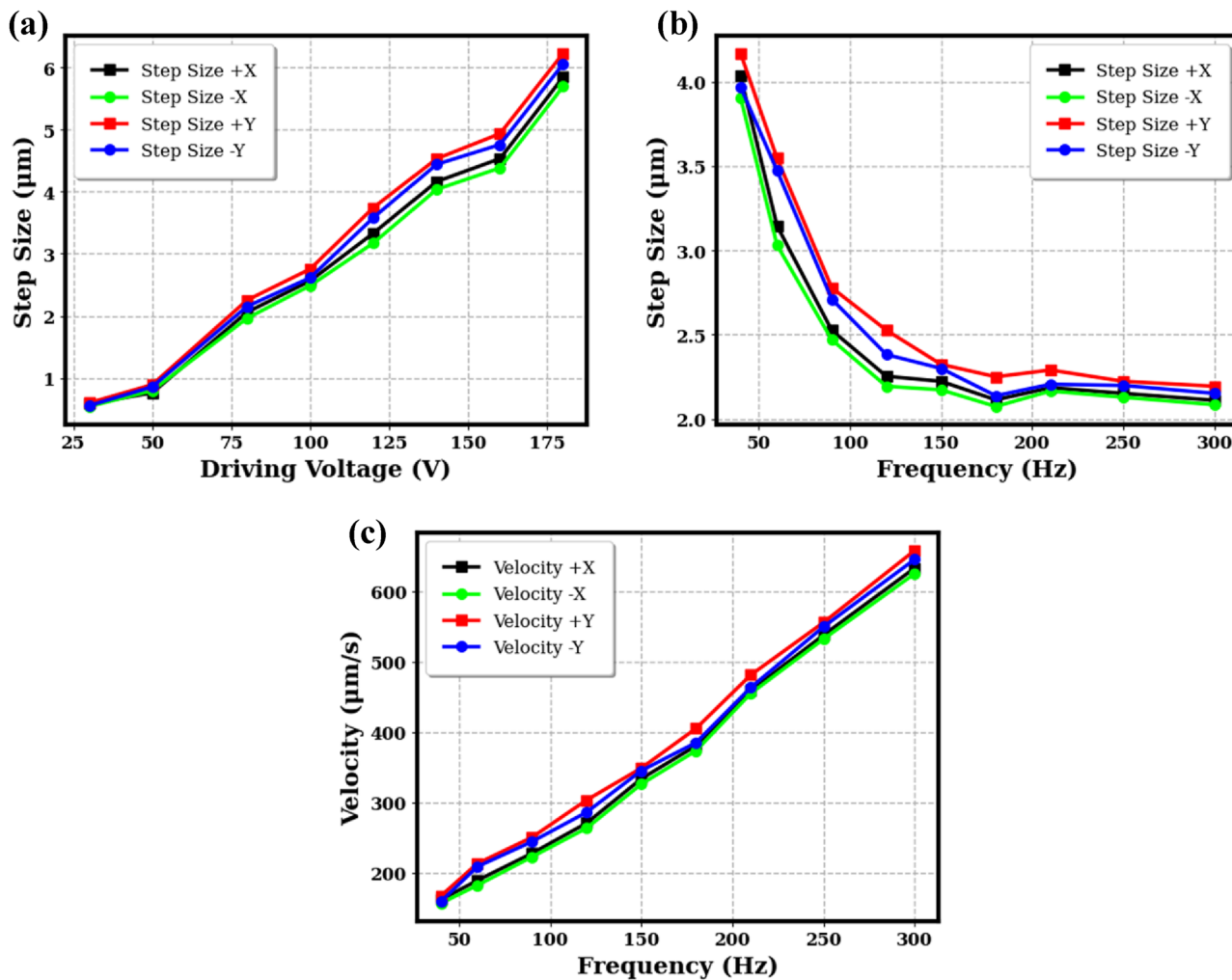


FIG. 4. (a) Step size vs driving voltage at Y+, Y-, X+, and X- directions with the frequency of 150 Hz. (b) Step size vs frequency with a constant driving voltage of 90 V. (c) Velocity vs frequency with a constant driving voltage of 90 V.

for the X axis and 0.47% for the Y axis, demonstrating consistent and acceptable variability in measurements. The slightly higher uncertainty in the Y axis suggests marginally less consistent performance along this direction, though it remains within acceptable limits for precision applications. Moreover, the energy loss of the motor, represented by the area enclosed in the hysteresis loop, is a measure of the energy dissipated as heat or other inefficiencies during each operational cycle. The X axis shows an energy loss of 0.02979 J, while the Y axis exhibits a slightly lower energy loss of 0.0283 J. This highlights the stability of the symmetric structure of PEM, material selection, and time-delayed control strategy of the driving signal in minimizing nonlinear effects. In future work, we will focus on advanced hysteresis modeling for this PEM and implement compensation techniques to further enhance its performance.

Additionally, the PEM's capability was assessed by measuring its load capacity. The step size of the motor was measured under

varying loads (0–120 g) at a fixed driving voltage of 180 V and a frequency of 150 Hz. As shown in Fig. 6(a), the step size decreases with the increasing load, reflecting the motor's reduced displacement capability due to increased friction and material deformation. At load 120 g with maximum voltage 180 V and frequency 150 Hz, the step size reached its minimum value (+X = 3.56 μm , -X = 3.45 μm , +Y = 3.87 μm , -Y = 3.65 μm), indicating that the motor is approaching its operational limit. These results highlight the motor's reliable performance up to 120 g and support the recommendation to avoid operation beyond this load. The photograph of PEM under load (120 g) is depicted in Fig. 6(b). It was observed that the motor continued to operate effectively with a 120 g load when a driving voltage of 180 V and a signal frequency of 150 Hz were applied and traversed a $10 \times 10 \text{ mm}^2$ area. Beyond this load, the motor leads to a point where it no longer functions effectively, reduced stability, and non-uniform motion, making operation at higher loads

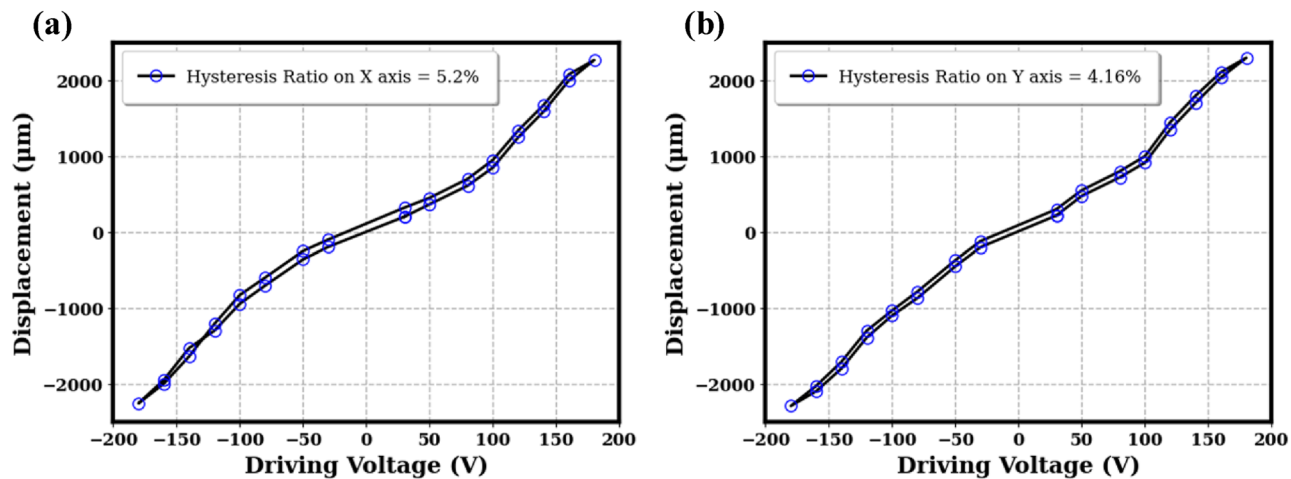


FIG. 5. Hysteresis characteristic of the PEM. (a) Hysteresis loop along the Y axis. (b) Hysteresis loop along the X axis.

unsuitable. Moreover, the load-dependent trends in hysteresis ratios were also analyzed as shown in Fig. 7. Analyzing load-dependent trends in hysteresis ratios is critical for evaluating the motor's accuracy, stability, and energy efficiency under varying loads.³⁴ As the load increases, the hysteresis ratio reflects the growing influence of friction, material deformation, and nonlinear behavior in the PEM. These trends highlight the motor's operational limits and guide the definition of maximum safe loads. The motor maintained stable operation up to 120 g, with hysteresis ratios remaining below 6.2% in the X plane and 5.2% in the Y plane, beyond which performance degrades due to excessive hysteresis and reduced step sizes. These findings indicate that the motor is well-suited for precision applications within its operational load range.

Furthermore, the long-term reliability of the PEM was demonstrated through continuous operation tests with a driving signal of 90 V and a frequency of 150 Hz over 12 h, during which the motor exhibited stable performance with no significant degradation and no significant changes in step sizes were observed in either the X or Y planes as shown in Fig. 8, confirming the reliability of the PEM. This durability extends its applicability to tasks requiring prolonged operation.

The sawtooth waveform combined with the time-delay-based control strategy ensures efficient and repeatable step motion. This approach achieves a consistent linear relationship between driving voltages and step sizes, a low threshold voltage (18 V), low hysteresis ratios (5.2% in X and 4.16% in Y), and smooth operation and

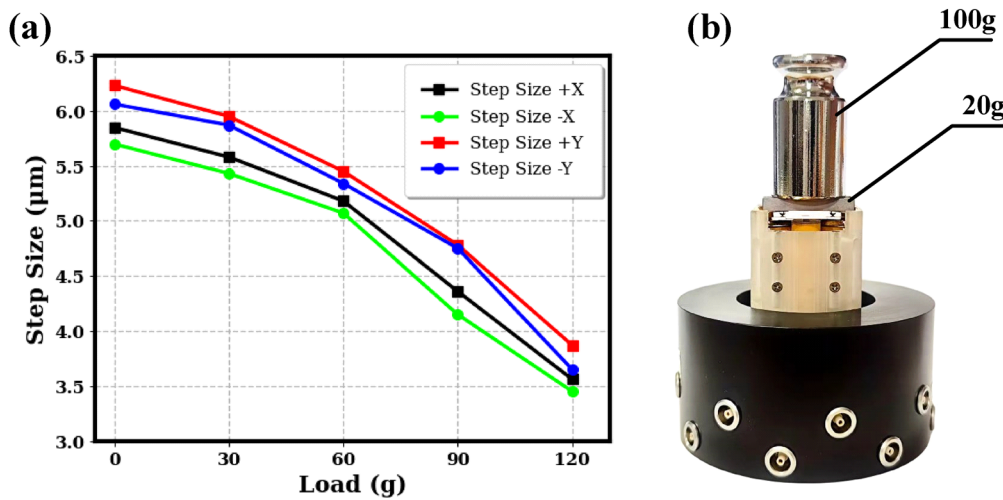


FIG. 6. (a) Step sizes vs different loads. (b) Photograph of the motor under load (120 g).

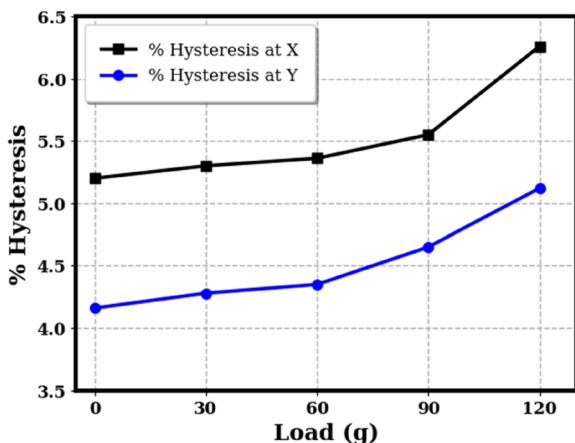


FIG. 7. Hysteresis ratio at the X and Y plane across different loads.

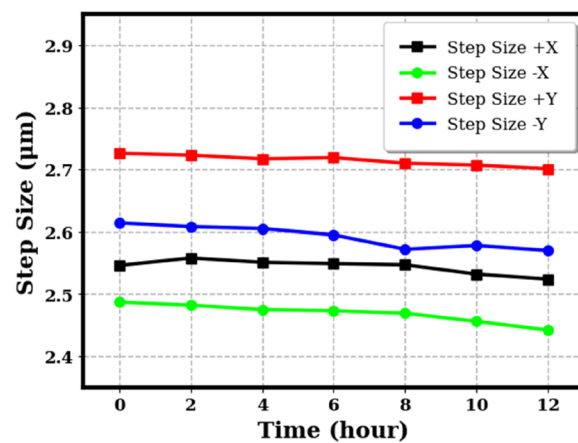


FIG. 8. Step sizes of the PEM in X and Y directions over 12 h at 90 V and 150 Hz.

stability during high-load conditions, even without advanced compensation techniques. Therefore, this signal was chosen because of its ability to provide smooth and controlled deformation of the PTs.

In future work, due to acceptable stability and accuracy, this MDOF PEM will be modified for applications such as achieving

atomic-resolution imaging or analyzing the magnetic properties of materials under ambient conditions and at low temperatures with superconducting magnets. Before its use in such extreme environments, it is essential to calculate the eigenfrequencies of the sapphire body to prevent resonance, excessive vibration, noise, and potential

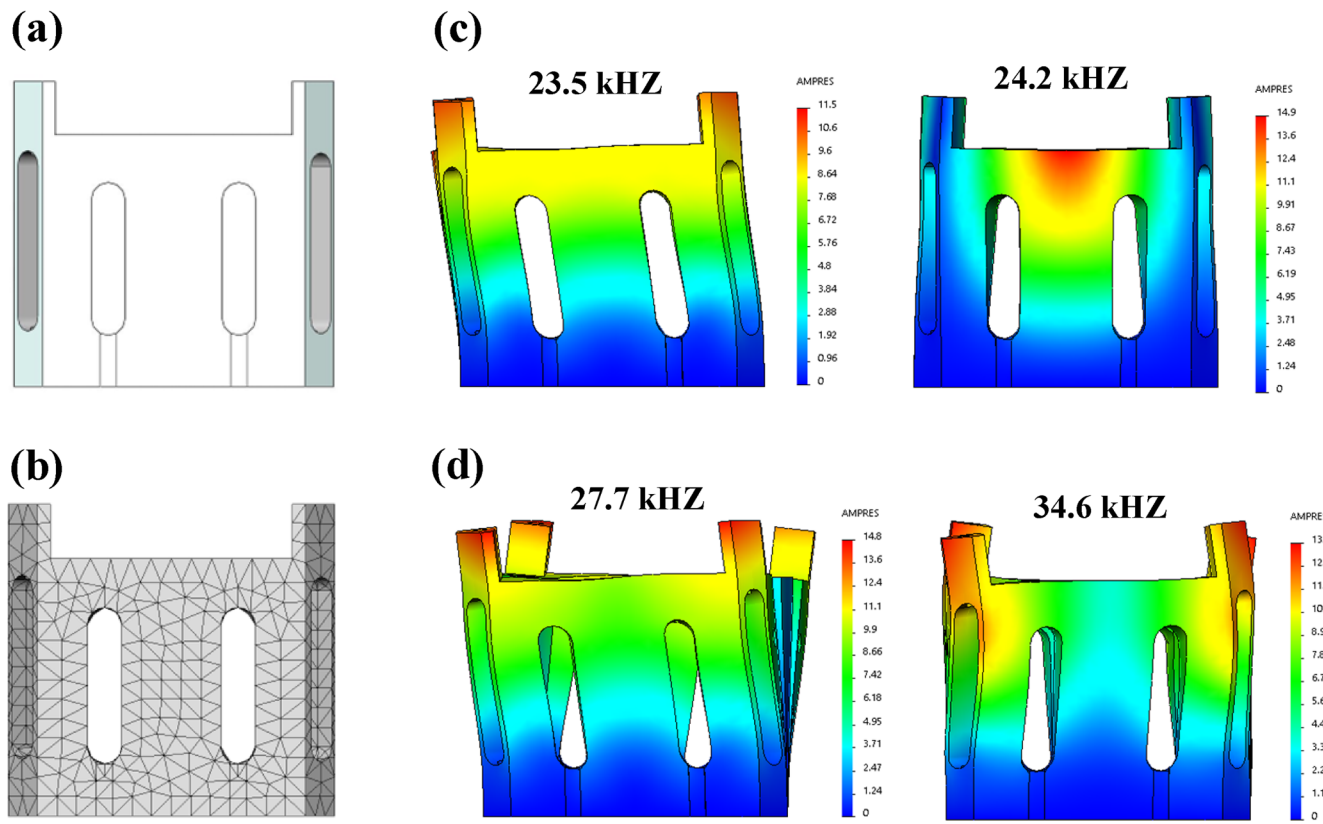


FIG. 9. (a) 3D rendered sapphire main body. (b) Mesh for FEA. (c) Eigenfrequencies of the sapphire main body at the bending mode and (d) torsional mode.

motor damage. Figures 9(a)–9(d) illustrate the Finite Element Analysis (FEA) used to determine the eigenmodes and eigenfrequencies of the primary sapphire frame. The specific design of the sapphire body has eigenfrequencies of 23.5 and 24.2 kHz in the bending mode and 27.7 and 34.6 kHz in the torsional mode. These findings confirm that the PEM can be safely operated in harsh conditions without compromising its integrity or performance. Additionally, its strong insulating properties allow it to effectively block magnetic field ripples, thereby preventing eddy current coupling. As a result, it mitigates temperature instability caused by eddy current heating during the field augmentation process.

V. CONCLUSION

This study introduced a novel MDOF piezoelectric motor (PEM) designed to address limitations in precision positioning systems. The innovative motor featured a compact structure ($33 \times 33 \times 30 \text{ mm}^3$) utilizing four piezoelectric tubes clamped by sapphire balls, supported by copper beryllium springs to ensure smooth and precise bidirectional movement. By implementing a sawtooth waveform with a time-delay control strategy, the motor achieved consistent step sizes ranging from 0.5 to 6 μm and maintained a low threshold voltage of 18 V. Hysteresis analysis revealed minimal energy loss, with ratios of 5.2% on the X axis and 4.16% on the Y axis, demonstrating high precision and efficiency. The motor reliably operated under loads up to 120 g and sustained stable performance over extended periods, indicating the motor's stability and any potential drift over time. The study's innovative design and performance metrics significantly advanced the capabilities of MDOF PEMs in precision positioning applications, such as superconducting magnets, with future improvements aimed at making it useful to achieve large-area atomic resolution imaging or magnetic properties of materials.

ACKNOWLEDGMENTS

This work was supported by the National Key R&D Program of China (Grant No. 2023YFA1607701), the National Natural Science Foundation of China (Grant Nos. 51627901 and 12374225), and the Maintenance and Renovation Project for CAS Major Scientific and Technological Infrastructure (Grant No. DSSWXGZ-2021-0006). We thank the staff members of the SMA System (<https://cstr.cn/31125.02.SHMFF.SM2.SMA>) at the Steady High Magnetic Field Facility, CAS (<https://cstr.cn/31125.02.SHMFE>), for providing technical support and assistance in data collection and analysis.

AUTHOR DECLARATIONS

Conflict of Interest

The authors have no conflicts to disclose.

Author Contributions

Syed Asad Maqbool: Conceptualization (equal); Data curation (equal); Formal analysis (equal); Investigation (equal); Methodology (equal); Software (equal); Visualization (equal); Writing – original draft (equal). **Muhammad Touqueer:** Conceptualization

(equal); Formal analysis (equal); Methodology (equal); Software (equal). **Behnam Esmaeilzadeh:** Data curation (equal); Investigation (equal); Methodology (equal). **Shiwei Yang:** Formal analysis (equal); Methodology (equal); Software (equal). **Wenjie Meng:** Conceptualization (equal); Formal analysis (equal); Methodology (equal). **Jihao Wang:** Data curation (equal); Formal analysis (equal); Validation (equal). **Qiyuan Feng:** Data curation (equal); Formal analysis (equal); Validation (equal). **Yubin Hou:** Funding acquisition (equal); Project administration (equal); Resources (equal). **Qingyou Lu:** Funding acquisition (equal); Investigation (equal); Resources (equal); Supervision (equal); Writing – review & editing (equal).

DATA AVAILABILITY

The data that support the findings of this study are available from the corresponding authors upon reasonable request.

REFERENCES

- ¹J. Guo, S. K. Chee, T. Yano, and T. Higuchi, *Sens. Actuators A* **194**, 119 (2013).
- ²H. Lu, W. Shang, H. Xie, and Y. Shen, *IEEE Trans. Rob.* **34**, 497 (2018).
- ³W. Yu-Jen, L. Chien, J. Yi-Bin, and F. Kuo-Chieh, *Smart Mater. Struct.* **26**, 065004 (2017).
- ⁴W.-L. Zhu, Z. Zhu, Y. He, K. F. Ehmann, B.-F. Ju, and S. Li, *IEEE/ASME Trans. Mechatron.* **22**, 1796 (2017).
- ⁵M. Touqueer, B. Esmaeilzadeh, W. Meng, J. Wang, S. A. Maqbool, S. Zheng, L. Junwei, Y. Hou, and Q. Lu, *Ultramicroscopy* **263**, 113983 (2024).
- ⁶B. Esmaeilzadeh, M. Touqueer, L. Junwei, S. Zheng, T. Geng, Y. Hou, and Q. Lu, *J. Microsc.* **294**, 26 (2024).
- ⁷M. Zhang, J. Wang, W. Meng, J. Zhang, Q. Feng, Z. Wang, Y. Lu, Y. Hou, and Q. Lu, *Rev. Sci. Instrum.* **95**, 033704 (2024).
- ⁸L. Šišovas, A. Čeponis, and S. Borodinas, *Proceedings of Actuators* (MDPI, 2024).
- ⁹Z. Li, Z. Su, H. Wang, S. Du, and H. Sun, *Sensors* **22**, 3739 (2022).
- ¹⁰V. Jürénas, G. Kazokaitis, and D. Mažeika, *Sensors* **20**, 834 (2020).
- ¹¹Q. Chang, W. Chen, S. Zhang, J. Deng, and Y. Liu, *Adv. Intell. Syst.* **6**, 2300780 (2024).
- ¹²M. Touqueer, S. A. Maqbool, B. Esmaeilzadeh, S. Zheng, W. Meng, A. Abas, J. Wang, Q. Feng, Y. Hou, and Q. Lu, *Rev. Sci. Instrum.* **95**, 083710 (2024).
- ¹³X. Gao, J. Yang, J. Wu, X. Xin, Z. Li, X. Yuan, X. Shen, and S. Dong, *Adv. Mater. Technol.* **5**, 1900716 (2020).
- ¹⁴S. Mohith, A. R. Upadhyaya, K. P. Navin, S. M. Kulkarni, and M. Rao, *Smart Mater. Struct.* **30**, 013002 (2020).
- ¹⁵S. Zheng, J. Wang, W. Meng, J. Zhang, Q. Feng, Z. Wang, Y. Hou, Q. Lu, and Y. Lu, *Rev. Sci. Instrum.* **93**, 043710 (2022).
- ¹⁶Z. Li, X. Chen, H. Zhao, J. Wang, S. Du, X. Guo, and H. Sun, *Micromachines* **13**, 967 (2022).
- ¹⁷Z. Li, K. Wang, H. Wang, X. Chen, X. Guo, and H. Sun, *Sensors* **23**, 6264 (2023).
- ¹⁸D. Berry, T. V. K. Vo, K. H. H. Li, T. M. Lubecki, and A. Gupta, *Sens. Actuators A* **358**, 114439 (2023).
- ¹⁹L. Wang, Y. Liu, J. Deng, X. Tian, and J. Liu, *Mech. Syst. Signal Process.* **135**, 106424 (2020).
- ²⁰L. Wang, D. Chen, T. Cheng, P. He, X. Lu, and H. Zhao, *Smart Mater. Struct.* **25**, 085033 (2016).
- ²¹M.-H. Park, H.-H. Chong, B.-H. Lee, S.-S. Jeong, and T.-G. Park, *Ferroelectrics* **500**, 218 (2016).
- ²²X. Ma, J. Liu, S. Zhang, J. Deng, and Y. Liu, *Sens. Actuators A* **364**, 114830 (2023).
- ²³S. Zhang, Y. Liu, J. Deng, X. Tian, and X. Gao, *Mech. Syst. Signal Process.* **149**, 107213 (2021).
- ²⁴Y. Liu, L. Wang, Z. Gu, Q. Quan, and J. Deng, *IEEE Trans. Ind. Electron.* **66**, 3030 (2019).

- ²⁵H. Jin, X. Gao, K. Ren, L. Qiao, J. Liu, Q. Li, R. Liu, N. Jia, S. Xia, S. Yang, and F. Li, *Mech. Syst. Signal Process.* **224**, 112157 (2025).
- ²⁶J. Nichols and K.-W. Ng, *Rev. Sci. Instrum.* **82**, 013706 (2011).
- ²⁷X. Zhou, S. Wu, X. Wang, Z. Wang, Q. Zhu, J. Sun, P. Huang, X. Wang, W. Huang, and Q. Lu, *Front. Mech. Eng.* **19**, 6 (2024).
- ²⁸P. Panda and B. Sahoo, *Micro and Smart Devices and Systems* (Springer, 2014).
- ²⁹J. Wang and Q. Lu, *Rev. Sci. Instrum.* **83**, 093701 (2012).
- ³⁰W. Meng, K. Zhao, J. Wang, J. Zhang, Q. Feng, Z. Wang, T. Geng, T. Guo, Y. Hou, L. Pi *et al.*, *Ultramicroscopy* **212**, 112975 (2020).
- ³¹K. Zhao, Y. Hou, S. Zheng, J. Wang, Y. Lu, W. Meng, and Q. Lu, *Smart Mater. Struct.* **32**, 055023 (2023).
- ³²J. Li, X. Zhou, H. Zhao, M. Shao, P. Hou, and X. Xu, *Smart Mater. Struct.* **24**, 065007 (2015).
- ³³K. Uchino, J. H. Zheng, Y. H. Chen, X. H. Du, J. Ryu, Y. Gao, S. Ural, S. Priya, and S. Hirose, *J. Mater. Sci.* **41**, 217 (2006).
- ³⁴H. H. Najafabadi, S. M. Rezaei, S. S. Ghidary, M. Zareinejad, K. Razi, and R. Seifabadi, in *Proceedings of 2007 IEEE/RSJ International Conference on Intelligent Robots and Systems* (IEEE, 2007).